

# Reconstructed *Homo habilis* type OH 7 suggests deep-rooted species diversity in early *Homo*

Fred Spoor<sup>1,2\*</sup>, Philipp Gunz<sup>1\*</sup>, Simon Neubauer<sup>1</sup>, Stefanie Stelzer<sup>1</sup>, Nadia Scott<sup>1</sup>, Amandus Kwekason<sup>3</sup> & M. Christopher Dean<sup>2</sup>

Besides *Homo erectus* (*sensu lato*), the eastern African fossil record of early *Homo* has been interpreted as representing either a single variable species, *Homo habilis*<sup>1</sup>, or two species<sup>2–6</sup>. In the latter case, however, there is no consensus over the respective groupings, and which of the two includes OH 7, the 1.8-million-year-old *H. habilis* holotype<sup>7</sup>. This partial skull and hand from Olduvai Gorge remains pivotal to evaluating the early evolution of the *Homo* lineage, and by priority names one or other of the two taxa. However, the distorted preservation of the diagnostically important OH 7 mandible has hindered attempts to compare this specimen with other fossils<sup>8,9</sup>. Here we present a virtual reconstruction of the OH 7 mandible, and compare it to other early *Homo* fossils. The reconstructed mandible is remarkably primitive, with a long and narrow dental arcade more similar to *Australopithecus afarensis* than to the derived parabolic arcades of *Homo sapiens* or *H. erectus*. We find that this shape variability is not consistent with a single species of early *Homo*. Importantly, the jaw morphology of OH 7 is incompatible with fossils assigned to *Homo rudolfensis*<sup>8</sup> and with the A.L. 666-1 *Homo* maxilla. The latter is morphologically more derived than OH 7 but 500,000 years older<sup>10</sup>, suggesting that the *H. habilis* lineage originated before 2.3 million years ago, thus marking deep-rooted species diversity in the genus *Homo*. We also reconstructed the parietal bones of OH 7 and estimated its endocranial volume. At between 729 and 824 ml it is larger than any previously published value, and emphasizes the near-complete overlap in brain size among species of early *Homo*. Our results clarify the *H. habilis* hypodigm, but raise questions about its phylogenetic relationships. Differences between species of early *Homo* appear to be characterized more by gnathic diversity than by differences in brain size, which was highly variable within all taxa.

Computed tomography (CT) reveals that distortion of the OH 7 mandible mostly involves a small number of fractures and displacements, without evidence of larger-scale plastic deformation (Fig. 1a). In a CT-based virtual reconstruction the individual parts of the corpus were therefore realigned by simple repositioning. The dental arcade from the left M<sub>2</sub> to the right M<sub>1</sub> was restored using combined clues from the interstitial facets, the alveoli and the observation that the displacement of the incisors occurred along a single transverse crack through their roots (Fig. 1d and Extended Data Figs 1–3). The dislocated right corpus covers a well-preserved lingual symphyseal surface with a marked genial spine and bilateral genioglossal pits (Fig. 1c). These features and the symmetrically placed apical halves of the I<sub>1</sub> roots jointly mark the midsagittal plane (Fig. 1b). Using this plane a second reconstruction was made by mirror-imaging the left side from M<sub>2</sub> to C to the right (Fig. 1f). The CT scans show that root formation of the C and M<sub>2</sub> was incomplete (Fig. 1c; contrary to ref. 9), confirming the original suggestion that OH 7 was a late juvenile<sup>11</sup>, rather than an adult<sup>12</sup> (Supplementary Note 1). Conclusions formed on the basis of the specific morphological analyses presented below are unlikely to be affected by the sub-adult status of OH 7 and some other early *Homo* fossils (Extended Data Figs 4 and 5 and Supplementary Note 2).

The two mandibular reconstructions of OH 7 are characterized by relatively long and parallel post-canine tooth rows. This primitive morphology contrasts with several other early *Homo* specimens, which show derived parabolic arcade shapes (Extended Data Fig. 6). We therefore test whether this shape variability is consistent with a single species of early *Homo* (*H. erectus*, following ref. 13). Alternative evolutionary scenarios invoke multiple species of early *Homo* that differ, at least, in dental arcade shape. We used geometric morphometrics to quantify the shape variability of dental arcade shape in early *Homo*, in the context of (1) the

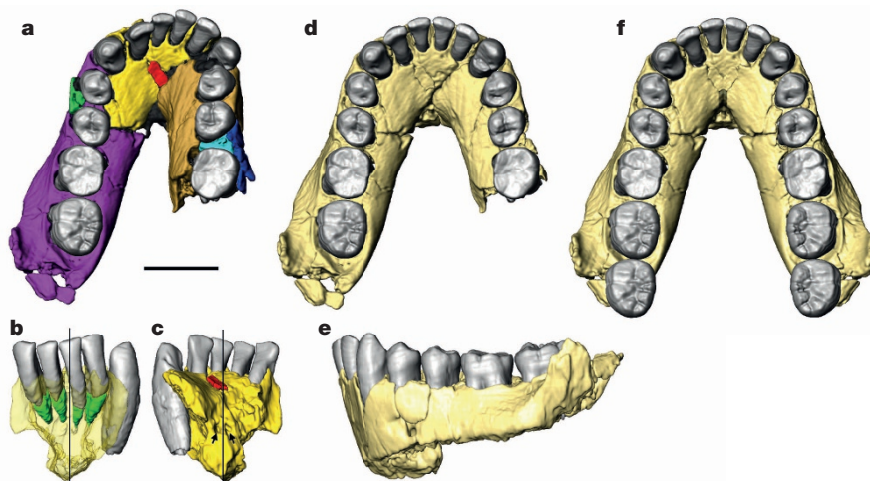


**Figure 1 | CT-based visualization of the OH 7 mandible.** **a**, As preserved, marking individual parts that were adjusted in the reconstruction. **b**, **c**, The anterior corpus showing the midsagittal plane in relation to the incisor roots (**b**, transparent, anterior view), and the genial spine and pits (**c**, posterior view; arrows indicate pits). **d**, **e**, The reconstructed mandible in occlusal and left lateral views, respectively. **f**, The mandible reconstructed using the mirror-imaged left corpus; M<sub>2</sub>s duplicated as M<sub>3</sub>s, and a small damaged area in the midline of the post-incisive plane shaded. Scale bar is 2 cm.

<sup>1</sup>Department of Human Evolution, Max Planck Institute for Evolutionary Anthropology, 04103 Leipzig, Germany. <sup>2</sup>Department of Cell and Developmental Biology, University College London, London WC1E 6BT, UK. <sup>3</sup>Museum and House of Culture, National Museum of Tanzania, Dar es Salaam, Tanzania.

\*These authors contributed equally to this work.

within-group shape variability of extant apes and humans, and (2) the effect of allometry on dental arcade shape. These analyses show that the shape of the OH 7 arcade is close to that of the early *Homo* mandibles KNM-ER 1802 and OH 13, and is more similar to shapes found in great apes and *Australopithecus* than in *H. sapiens* (Fig. 2a and Extended Data Figs 4 and 5). Compared with other early *Homo* specimens it strongly contrasts with mandibles of *H. erectus* and with KNM-ER 1482 and KNM-ER 60000, specimens that have been associated with the iconic cranium KNM-ER 1470 (ref. 8; Fig. 2a, b). This difference is as large as between *Gorilla gorilla* and *Pan troglodytes*. When specimens are attributed to *H. habilis* (OH7, OH 13, KNM-ER 1802), *H. erectus* (Dmanisi) and *H. rudolfensis* (KNM-ER 1482, KNM-ER 60000; following ref. 8) the respective within-group shape variations are consistent with those shown by extant hominids (Fig. 2c). In contrast, pooling any of these early *Homo* groups yields shape distances that far exceed those found in extant species, and distributions are mostly bimodal (Fig. 2c). We found no static allometric effects on dental arcade shape (Extended Data Fig. 7).

To compare OH 7 with key maxillae attributed to early *Homo* we predicted the shape of its maxillary dental arcade using multiple multivariate regression analysis, on the basis of the strong and consistent pattern of covariation between the maxillary and mandibular dental arcade shapes of extant humans and great apes (Extended Data Figs 8 and 9). In addition, we manually reconstructed the maxillary arcade of OH 7 on the basis of an occlusal match between lower and upper tooth crowns (Extended

Data Fig. 6c). The predicted maxillary arcade follows the same morphological pattern as the mandible, is most similar in shape to that of *A. afarensis*, and is different from those of other early *Homo* maxillae (Fig. 2d, e and Extended Data Figs 4 and 5). The inferred OH 7 maxilla is most similar to KNM-ER 1813, but at the extreme boundaries of the intraspecific shape differences found between two individuals in extant humans and great apes (Fig. 2e). The difference between the *H. erectus* maxilla D2282 and OH 7 falls just within the 95% boundary of *G. gorilla*, but the better preserved mandible D211 of the same individual clearly differs from OH 7 (Fig. 2c). OH 7 is most distinct from KNM-ER 62000, a specimen that closely resembles KNM-ER 1470 (ref. 8). This shape difference is as large as that between some extant *H. sapiens* and *Pan troglodytes* individuals (Fig. 2e) and variation of the pooled early *Homo* sample well exceeds that of extant hominid taxa (Extended Data Fig. 5a).

The left and right parietal bones of OH 7 are both incomplete, but bilaterally preserved parts complement each other<sup>1</sup>, enabling reconstruction of the entire parietal portion of the vault (Fig. 3a, b and Extended Data Fig. 10). In extant humans and great apes the endocranial volume (ECV) is strongly correlated with the form (combined shape and size) of the parietal endocranial surface. Using this relationship and two methods we estimated four separate ECVs from the reconstructed OH 7 parietals, with values between 729 and 824 ml (combined uncertainty range 630–967 ml). These ECVs are considerably larger than previous estimates<sup>1,14–20</sup>, typically given as 647–687 ml<sup>1,20</sup> (Fig. 3c). We consider our values more reliable as they are calculated on the basis of larger and taxonomically

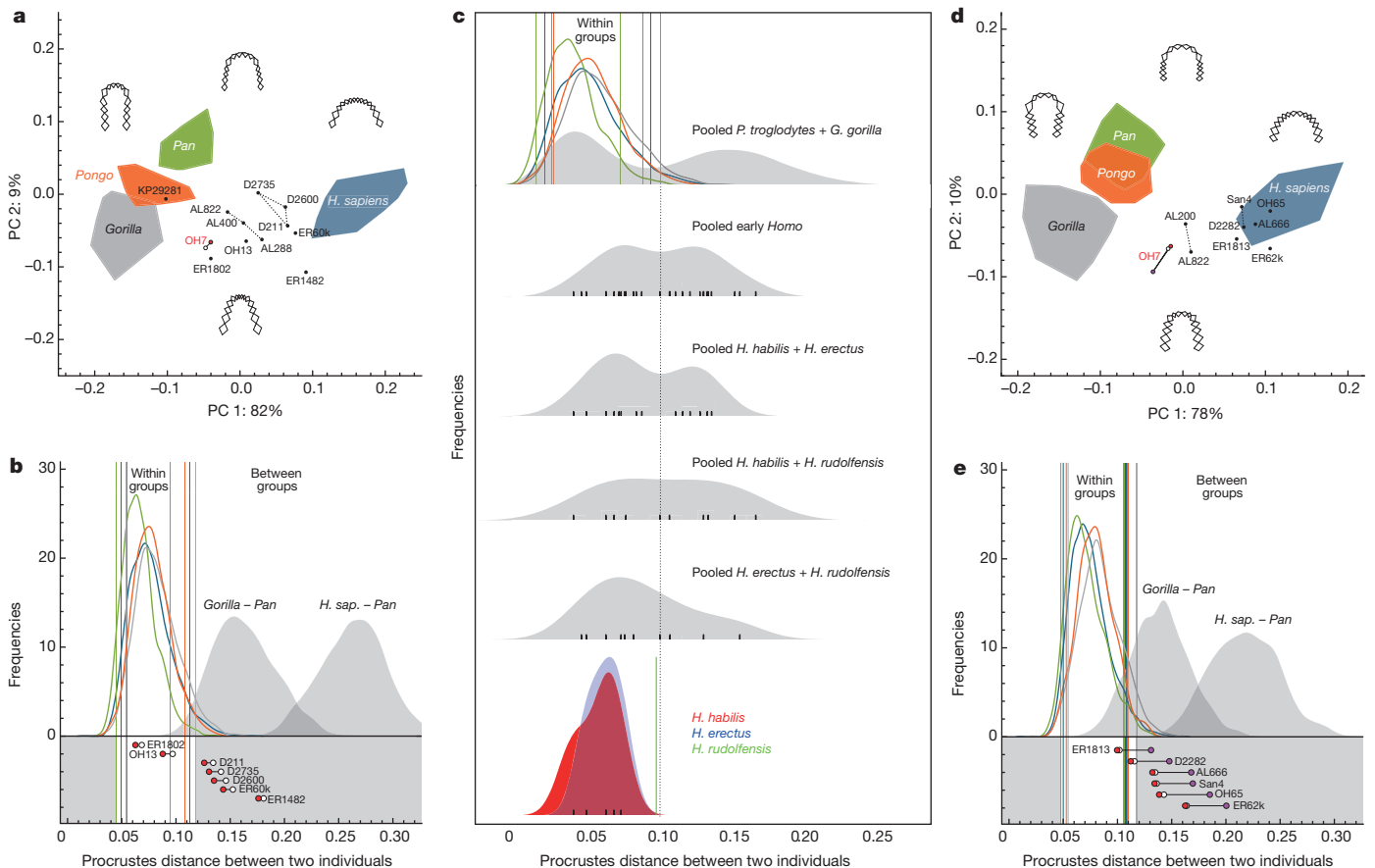


**Figure 2 | Analysis of the OH 7 jaw.** **a**, Plot of principal components (PC) 1 and 2 describing the shape of the mandibular dental arcade; associated shape changes three standard deviations away from the mean are shown. OH 7 is represented by the full-corpus (red) and symmetry-based (white) reconstructions. **b**, Procrustes distances between OH 7 and other early *Homo* mandibles compared to frequency plots of distances between all possible individual pairs within and between extant groups (colours as in **a**; lines represent 5% and 95% limits of intraspecific distributions). **c**, Frequency plots

of the mandibular shape differences between all pairs within extant groups (as in **b**), a pooled sample of chimps and gorillas (top), and various groupings of early *Homo* fossils (lower five), with black ticks showing the distance between each pair. **d**, Same as **a** for maxillary shape. For OH 7 the two statistical predictions and one anatomical prediction (purple) are plotted. **e**, Same as **c** for pairwise shape differences between maxillae. As in **d** three reconstructions of OH 7 are plotted.

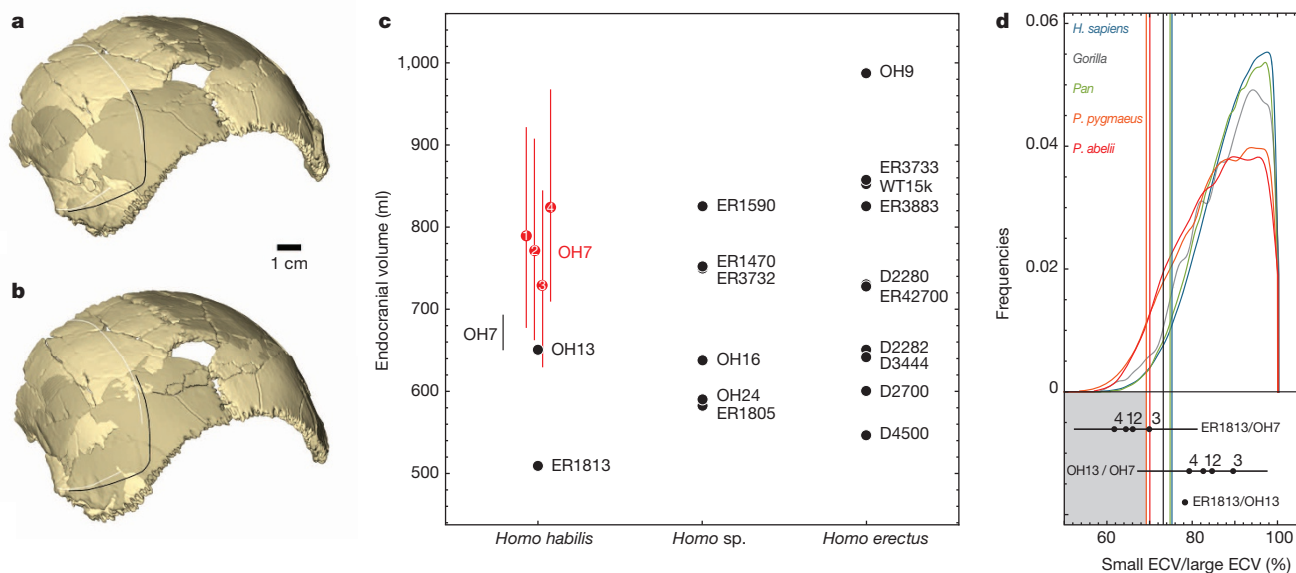


**Figure 3 | Reconstruction and analysis of the OH 7 parietals.** **a, b**, Two alternative anatomical reconstructions in posterolateral view, with temporal lines shown in white (left side) and black (mirrored right side), mirror-imaged bones in darker shade. **c**, Means and ranges of four ECV predictions for OH 7 (red 1 and 2, regression-based and geometric reconstruction based estimates for first anatomical reconstruction; red 3 and 4, corresponding estimates for

more diverse comparative samples, and the linear regression model is not taxon-dependent, performing equally well for great ape species and humans (Extended Data Fig. 10f).

The ECV estimates obtained for OH 7 fall well within the range of early *H. erectus* (546–1067 ml) and are among the largest values reported for other specimen attributed to early *Homo*<sup>13,20</sup> (Fig. 3c). Specimens that show affinities with OH 7 in dental arcade shape and have estimated ECVs are OH 13 and KNM-ER 1813. The difference in ECV between OH 13 (650 ml, ref. 15) and OH 7 falls well within the intraspecific variation of extant hominids (Fig. 3c). The difference between KNM-ER 1813 (509 ml, ref. 20) and OH 7 is substantially larger, and can only be sampled in extant humans and great apes when the lower ECV predictions are considered for OH 7.

The reconstructed mandible and parietals of OH 7 reveal that the holotype of *H. habilis* is characterized by primitive gnathic morphology; a long and narrow dental arcade indicative of a subnasally prognathic face, combined with a larger ECV than assumed thus far. Analysing shape variation of the dental arcades shows that the early *Homo* sample represents more than one species (contrary to ref. 13), and that a *H. habilis* hypodigm of OH 7 combined with KNM-ER 1802 and OH 13 is consistent with intraspecific variation seen in extant hominids (Fig. 2c). Both gnathic and parietal evidence indicate that it is possible that KNM-ER 1813 is also part of this hypodigm. If so, *H. habilis* would have been variable, suggesting considerable sexual dimorphism as well as evolutionary changes over the documented temporal range of these specimens from 2 million years (Myr) to 1.65 Myr ago<sup>21,22</sup>.

In terms of arcade shape OH 7 is most distinct from the partial cranium KNM-ER 62000 and the mandible KNM-ER 1482. These specimens have both been associated with KNM-ER 1470, and are marked by shorter post-canine tooth rows and a non-projecting anterior row<sup>9</sup>. The KNM-ER 1470 maxilla is incompletely preserved and could not be included in the analyses, but visual comparison with OH 7 nevertheless suggests a comparable difference in arcade shape (Extended Data Fig. 6h, i). This major difference in gnathic morphology fully supports the view that KNM-ER 1470 and associated specimens are best attributed to a species other than *H. habilis* (contrary to ref. 13) for which the name *H. rudolfensis* is available<sup>23</sup>. The mandible KNM-ER 60000 has been associated with KNM-ER 1470, KNM-ER 62000 and KNM-ER

second anatomical reconstruction), compared with typical values reported previously<sup>11,19</sup> (black), and with other early *Homo* specimens. **d**, Difference in ECV between OH 7, OH 13 and KNM-ER 1813 compared with pairwise intraspecific differences within extant hominid species as a ratio of the smaller ECV divided by the larger ECV. Lines represent the 5% limits of these distributions.

1482 (ref. 8), but the shape of its dental arcade shows the closest similarity to early *H. erectus* mandibles from Dmanisi rather than to KNM-ER 1482 (Fig. 2a). Clearly, the relationship between *H. rudolfensis* and early *H. erectus* warrants further quantitative analysis using an expanded landmark data set which comprehensively captures the facial features reported to characterize *H. rudolfensis*<sup>3,4,8</sup> but this lies beyond the scope and focus of this paper.

The maxillae OH 65 and A.L. 666-1 have been associated with *H. habilis*<sup>6,10</sup>. However, considered by the standards of intraspecific variation among extant hominids, their morphology is incompatible with OH 7 (Fig. 2e), and hence *H. habilis*. Both are close to modern humans in dental arcade shape (Fig. 2d and Extended Data Fig. 4c, d), but lack the unique facial morphology used to diagnose *H. rudolfensis*<sup>8,10</sup>. Suggested similarities to early *H. erectus*<sup>13</sup> are consistent with the evidence presented here, but require further examination. Regardless of species affinities it is remarkable that the 2.3-Myr-old<sup>10</sup> A.L. 666-1 is 0.5 Myr older than OH 7, but is distinctly more derived in gnathic morphology. This pattern suggests that the *H. habilis* lineage originated before 2.3 Myr ago, predating the oldest fossil evidence for the genus *Homo*<sup>10</sup>. OH 13 shows that *H. habilis* survived until at least 1.65 Myr ago, but a previously reported last appearance date of 1.44 Myr<sup>21</sup> can no longer be demonstrated in light of new evidence presented here and elsewhere<sup>13</sup> (Supplementary Note 3).

Our new ECV estimates of OH 7 support the view that for the period between 2.1 and 1.5 Myr ago the ECVs of *H. habilis*, *H. rudolfensis* and *H. erectus* largely overlapped in range<sup>24</sup>, and broadly fell between 500 and 900 ml (Fig. 3c). Hence, although *H. erectus* shows autapomorphic features of the calvaria<sup>21</sup>, there is little evidence that the early radiation of the genus *Homo* was marked by interspecific diversification in brain size. In contrast, it is facial morphology that appears to distinguish these three species. The dental arcades of *H. habilis* show the most primitive morphology, with long and parallel post-canine dental rows suggestive of a subnasally prognathic face, as opposed to the more diverging and reduced post-canine rows seen in early *H. erectus*, *H. sapiens* and A.L. 666-1, the currently earliest known *Homo*. The dental arcade of the *H. rudolfensis* face KNM-ER 62000 also shows shorter post-canine rows, but these are more parallel, and the incisor row is distinctly flat and retracted along the bi-canine line (Extended Data Fig. 5b and



Supplementary Note 2). Brain size increase in the genus *Homo*, and *H. erectus* in particular, has been linked with a shift towards energy- and nutrient-rich diets and a reduced masticatory system<sup>25–28</sup>. Nevertheless, the *H. habilis* type specimen, OH 7, demonstrates that increased brain size, equivalent to that in early *H. erectus*, occurred in combination with a more primitive gnathic morphology without any signs of reduced dental size or corpus robusticity (Supplementary Note 4).

**Note added in proof:** The recently described LD 350-1 partial mandible from Ethiopia now provides the earliest evidence of the genus *Homo* at 2.8 Myr (Villmoare, B. *et al.* Early *Homo* at 2.8 Ma from Ledi-Geraru, Afar, Ethiopia. *Science*, in the press). Its morphology is more primitive than seen in the mandibles we attribute to *H. habilis*, and this new evidence supports the conclusions of our study.

**Online Content** Methods, along with any additional Extended Data display items and Source Data, are available in the online version of the paper; references unique to these sections appear only in the online paper.

Received 1 April 2014; accepted 8 January 2015.

- Tobias, P. V. *Olduvai Gorge Volume 4: The Skulls and Endocasts of Homo habilis* (Cambridge Univ. Press, 1991).
- Stringer, C. B. in *Major Topics in Primate and Human Evolution* (eds Wood, B., Martin, L. & Andrews, P.) 266–294 (Cambridge Univ. Press, 1986).
- Lieberman, D. E., Pilbeam, D. R. & Wood, B. A. A probabilistic approach to the problem of sexual dimorphism in *Homo habilis*: a comparison of KNM-ER 1470 and KNM-ER 1813. *J. Hum. Evol.* **17**, 503–511 (1988).
- Wood, B. Origin and evolution of the genus *Homo*. *Nature* **355**, 783–790 (1992).
- Rightmire, G. P. Variation among early *Homo* crania from Olduvai Gorge and the Koobi Fora region. *Am. J. Phys. Anthropol.* **90**, 1–33 (1993).
- Blumenschine, R. J. *et al.* Late Pliocene *Homo* and hominid land use from western Olduvai Gorge, Tanzania. *Science* **299**, 1217–1221 (2003).
- Leakey, L. S. B., Tobias, P. V. & Napier, J. R. A new species of the genus *Homo* from Olduvai Gorge. *Nature* **202**, 7–9 (1964).
- Leakey, M. G. *et al.* New fossils from Koobi Fora, northern Kenya, confirm taxonomic diversity in early *Homo*. *Nature* **488**, 201–204 (2012).
- Antón, S. C., Potts, R. & Aiello, L. C. Evolution of early *Homo*: an integrated biological perspective. *Science* **345** (2014).
- Kimbel, W. H., Johanson, D. C. & Rak, Y. Systematic assessment of a maxilla of *Homo* from Hadar, Ethiopia. *Am. J. Phys. Anthropol.* **103**, 235–262 (1997).
- Leakey, L. S. B. New finds at Olduvai Gorge. *Nature* **189**, 649–650 (1961).
- Schwartz, J. H. & Tattersall, I. *The human fossil record*, Vol. 2 (Wiley-Liss, 2003).
- Lordkipanidze, D. *et al.* A complete skull from Dmanisi, Georgia, and the evolutionary biology of early *Homo*. *Science* **342**, 326–331 (2013).
- Tobias, P. V. Cranial capacity in anthropoid apes, *Australopithecus* and *Homo habilis*, with comments on skewed samples. *S. Afr. J. Sci.* **64**, 81–91 (1968).
- Holloway, R. L. New endocranial values for the East African early hominids. *Nature* **243**, 97–99 (1973).
- Holloway, R. L. The OH 7 (Olduvai Gorge, Tanzania) hominid partial brain endocast revisited. *Am. J. Phys. Anthropol.* **53**, 267–274 (1980).
- Wolpoff, M. H. Cranial capacity estimates for Olduvai Hominid 7. *Am. J. Phys. Anthropol.* **56**, 297–304 (1981).
- Holloway, R. L. The OH 7 (Olduvai Gorge, Tanzania) parietal fragments and their reconstruction: a reply to Wolpoff. *Am. J. Phys. Anthropol.* **60**, 505–516 (1983).
- Vaišnyš, J. R., Lieberman, D. & Pilbeam, D. An alternative method of estimating the cranial capacity of Olduvai Hominid 7. *Am. J. Phys. Anthropol.* **65**, 71–81 (1984).
- Holloway, R. L., Broadfield, D. C. & Yuan, M. S. *The human fossil record*, Vol. 3 (Wiley-Liss, 2004).
- Spoor, F. *et al.* Implications of new early *Homo* fossils from Ileret, east of Lake Turkana, Kenya. *Nature* **448**, 688–691 (2007).
- Joordens, J. C. A. *et al.* Improved age control on early *Homo* fossils from the upper Burgi Member at Koobi Fora, Kenya. *J. Hum. Evol.* **65**, 731–745 (2013).
- Wood, B. '*Homo rudolfensis*' Alexeev, 1986 – fact or phantom? *J. Hum. Evol.* **36**, 115–118 (1999).
- Lieberman, D. *Evolution of the human head* (Harvard Univ. Press, 2011).
- Wrangham, R. W., Holland Jones, J., Laden, G., Pilbeam, D. & Conklin-Brittain, N. The raw and the stolen. Cooking and the ecology of human origins. *Curr. Anthropol.* **40**, 567–594 (1999).
- Stedman, H. H. *et al.* Myosin gene mutation correlates with anatomical changes in the human lineage. *Nature* **428**, 415–418 (2004).
- Leonard, W. R., Snodgrass, J. J. & Robertson, M. L. Effects of brain evolution on human nutrition and metabolism. *Annu. Rev. Nutr.* **27**, 311–327 (2007).
- Jiménez-Arenas, J. M., Pérez-Claros, J. A., Aledo, J. C. & Palmqvist, P. On the relationships of postcanine tooth size with dietary quality and brain volume in primates: implications for hominin evolution. *BioMed Res. Int.* **2014**, 1–11 (2014).

**Supplementary Information** is available in the online version of the paper.

**Acknowledgements** We thank the National Museum of Tanzania, the Tanzania Commission for Science and Technology and the National Museums of Kenya for giving access to fossils in their care, and the Imaging Plus Medical Centre, Dar es Salaam, for CT scanning facilities. We are grateful to M. Leakey, L. Leakey, J.-J. Hublin and S. Antón for support and encouragement, and to R. Blumenschine, P. Corujo, R. David, P. Gokarn, W. Kimbel, K. Kupczik, R. Leakey, J. Lewis, E. Mbua, R. McCarthy, M. Meyer, P. Mitteroecker, P. Msemwa, J. Njau, D. Reinhardt, L. Schroeder, M. Skinner, A. Stoessel, A. Strauss, H. Temming and B. Wood for help with aspects of this study. Research was supported by the Max Planck Society.

**Author Contributions** F.S., S.N., S.S., N.S., A.K. and C.D. collected data. F.S., P.G., S.N. and C.D. performed analyses. F.S. wrote the paper, with contributions from P.G., S.N. and C.D.

**Author Information** Reprints and permissions information is available at [www.nature.com/reprints](http://www.nature.com/reprints). The authors declare no competing financial interests. Readers are welcome to comment on the online version of the paper. Correspondence and requests for materials should be addressed to F.S. ([f.spoor@ucl.ac.uk](mailto:f.spoor@ucl.ac.uk)) or P.G. ([gunz@eva.mpg.de](mailto:gunz@eva.mpg.de)).

## METHODS

**CT scanning.** In December 2010 OH 7 was CT scanned with a Siemens Somatom 4, using a slice collimation of 1.0 mm. The image stacks used for 3D visualizations were reconstructed with a voxel size of  $0.2 \times 0.2 \times 0.5$  mm, H70h kernel and extended CT scale. The reconstructions of the mandible and parietals use images in the transverse and coronal planes, respectively. OH 7X (right  $M_2$ ; ref. 29) is housed in the National Natural History Museum in Arusha rather than the Museum and House of Culture in Dar es Salaam, and was studied but not CT scanned. Specimens in the comparative sample were scanned with a medical CT scanner (parameters similar to those for OH 7) or with a BIR ACTIS 225/300 (Max Planck Institute for Evolutionary Anthropology, Leipzig), isotropic voxel size of 0.1 mm or less. Avizo 6.3-7.1 (Visualization Sciences Group) and Geomagic Studio 2013 (Geomagic Inc.) were used for visualization, segmentation, reconstruction and 3D landmarking.

**Reconstruction of the OH 7 mandible.** The reconstruction procedure is discussed in more detail in the Supplementary Methods. The OH 7 mandible was examined by F.S. and M.C.D. to map the pattern of externally visible cracks, displacements and crucial morphological details such as interstitial facets of the tooth crowns. This information was combined with the internal morphology as shown in CT images. The main distortion concerns displacement of teeth and corpus parts along three well-defined fractures: (1) labiolingually through the right C alveolus; (2) through the left corpus from  $P_4$  lingually to C labially; and (3) transversely through the anterior corpus and tooth roots, marking the dislocation of the I crowns (Extended Data Figs 1 and 2).

The 13 teeth and seven corpus parts were digitally separated, as colour coded in Extended Data Fig. 1. The fragmented buccal wall on the right and remnants of matrix were removed, and six corpus parts realigned, guided by their edges and surfaces. Subsequently, the incisors could be realigned, on the basis of the interstitial facets and the apical portion of their roots that remain in their original alveolar positions. The other teeth were repositioned on the basis of their interstitial facets and alveoli. Only the mesial half of the right corpus is preserved, and a second, more complete reconstruction was therefore made, using a copy of the left corpus instead. The latter was mirror-imaged across the midsagittal plane of the anterior corpus, marked by the genial spine and genioglossal pits on the posterior symphyseal surface in combination with the apical halves of the  $I_1$  roots (Fig. 1b, c). The right corpus surrogate thus obtained and the actual right corpus fragment are close in orientation, with the latter being 1 degree more divergent relative to the midsagittal plane. The good match between individual parts confirms that the corpus experienced little or no plastic deformation and that the estimated midsagittal plane is a good reflection of bilateral symmetry (Extended Data Fig. 2e). Finally, to facilitate visual comparisons of overall dental arcade shape the left  $M_2$  was used to represent the similarly sized right  $M_2$ , and the missing  $M_3$ s (Fig. 1f). However, the  $M_3$ s were not considered in any of the shape analyses of the dental arcade. Measurements of the mandibular reconstructions are given in Supplementary Note 5.

**Shape analyses of the mandibular and maxillary dental arcades.** Landmarks. Dental arcades were quantified using 3D landmarks, taken either directly from original specimens or casts with a Microscribe digitizer (Solution Technologies), or from digital volume or surface data using Avizo 6.3 or 7.1 (Visualization Sciences Group). Eighty landmarks are defined which describe the mesial, distal, lingual and buccal/labial alveolar margins of the maxillary and mandibular dental arcade from left to right  $M_3$  (Extended Data Fig. 2f, g). The mesial and distal roots of the molars and premolars were landmarked separately, but in the analyses their coordinates were averaged. Mesial and distal landmarks between the tooth crowns are difficult to reach with the Microscribe. These are therefore calculated from pairs of landmarks positioned slightly more buccally/labially and lingually. The  $M_3$ s of OH 7 are not preserved and analyses therefore use a subset of landmarks from left to right  $M_2$ . Results of comparative analyses with or without  $M_3$ s are not meaningfully different. For visualization the 43  $M_2$ -to- $M_2$  landmarks are connected by a wireframe. **Extant species.** Specimens are pairs of matching maxillae and mandibles, without distinct pathologies or malocclusion. Late juveniles are specimens similar in developmental age to OH 7, with erupted Cs and unerupted  $M_3$ s. The number of late juveniles that could be included was low because among modern *Homo sapiens* this age group is sparsely represented in museum collections, and among great apes this pattern of dental eruption is rare because eruption of the  $M_3$  usually precedes or coincides with eruption of the canine. To maximize sample sizes the late juveniles therefore include a few crania without mandibles.

*Homo sapiens*: adults 80, worldwide populations; late juveniles 7 maxillae, 5 mandibles. *Pan troglodytes*: adults 41, including *P. t. troglodytes*, *P. t. verus* and *P. t. schweinfurthii*; late juveniles 11 maxillae, 10 mandibles. *Gorilla gorilla*: adults 46; late juveniles 4 maxillae, 2 mandibles. *Pongo* sp.: adults 22.

**Fossil specimens.** Sample composition of early *Homo* reflects preservation of the dental arcade, a developmental age marked by erupted Cs, and availability of data. *Australopithecus* specimens were included to represent the ancestral or primitive state of gnathic morphology relative to the genus *Homo*. Specimens are labelled in

the graphs by their accession number, leaving off the prefix 'KNM-' for specimens housed in the National Museums of Kenya, and the designation '-1' for A.L. specimens housed in the National Museum of Ethiopia.

*Australopithecus anamensis* KNM-KP29281: CT scan. Landmarks taken from the right side and mirror imaged using the midsagittal plane of the symphysis.

*Australopithecus afarensis*: A.L. 200-1, A.L. 288-1 and A.L. 400-1: CT-based 3D surface of plaster casts (source: Cleveland Museum of Natural History). Missing landmark data for the left  $M_2$  of A.L. 288-1 estimated using reflected relabelling<sup>30</sup>. A.L. 822-1: casts of the reconstructed cranium and mandible<sup>31</sup>, courtesy of W. Kimbel and Y. Rak.

*Homo erectus*: D211, D2282, D2600, D 2735: CT-based 3D surface of casts (source: Georgian National Museum). The right side of D2282 landmarked and mirror-imaged using the midsagittal plane of the palate. Missing landmarks of the left  $P_4$  and  $M_1$  alveoli of D2600 mirror-imaged from the right and matched into the left tooth row on the basis of the shared  $P_3$  and  $M_3$  landmarks. Sangiran 4: CT scan. Landmarks taken from the right side and mirror-imaged using the midsagittal plane of the palate.

*Homo habilis*: OH 7: CT-based 3D reconstructions (this paper). Missing landmark data for the  $M_1$  (buccal, distal) and  $M_2$  (all) of the partial right corpus were estimated using reflected relabelling<sup>30</sup>. The second reconstruction employing mirror-imaging provides all landmarks.

*Homo* sp.: A.L. 666-1: orthogonal, parallel projected 3D surface views of a cast<sup>20</sup>. KNM-ER 1482: CT scan. Landmarks taken from the left side and mirror-imaged using the midsagittal plane of the symphysis. KNM-ER 1802, KNM-ER 60000, KNM-ER 62000: CT-based 3D reconstructions<sup>8</sup>. KNM-ER 1813: CT scan. The left  $P_3$  to  $M^2$  were mirror-imaged and matched into the right tooth row. Landmarks were taken from the right side and mirror-imaged using the midsagittal plane of the palate. OH 13: laser scan of the mandible, courtesy of L. Schroeder. OH 65: CT-based 3D surface of a cast, courtesy of R. Blumenshine and R. Leakey.

Prominent early *Homo* specimens not included: KNM-ER 992, 1470, 3733 and UR501 (insufficiently preserved), KNM-ER 730 (*in-vivo* infill and resorption of incisor alveoli), KNM-ER 1805 (maxilla with severe post-mortem distortion; mandible with deformed symphyseal area, likely associated with *in-vivo* loss of anterior dentition), KNM-WT 15000 (developmentally too young), OH 24 (insufficiently preserved and plastic deformation), and D2700 (multiple casts inconclusive regarding poorly preserved alveolar margins and palatal preservation).

Analyses were done using the full hominid sample as well as just the hominins (Fig. 2, Extended Data Figs 4 and 5 and Supplementary Note 2). This approach assesses the fossil hominins with and without the context of the strong morphological contrast between modern humans and great apes.

**Procrustes superimposition and principal component analysis.** As several fossil specimens were reconstructed using mirror-imaging, we symmetrized all specimens using reflected relabelling<sup>30,32</sup>. The symmetrized landmark coordinates were then converted to shape variables using generalized least squares Procrustes superimposition<sup>33</sup>. This superimposition standardizes position, orientation and scale; the resulting Procrustes coordinates were analysed using multivariate statistics. We used principal component analysis to reduce the dimensions of the high-dimensional data set. Landmarks on the maxilla and mandible were analysed separately. All geometric morphometric and statistical analyses were performed in Mathematica (Wolfram Research) using scripts written by P.G.

**Statistical prediction of OH 7 maxillary arcade.** So as to compare the dental arcade shape of OH 7 with relevant fossil specimens for which only maxillae exist, we estimated the shape of its maxillary arcade shape using two approaches: an anatomical prediction on the basis of crown occlusion, described below, as well as a statistical model<sup>30</sup> dependent on the covariation of the upper and lower jaw (Extended Data Fig. 8). For the latter we computed five multiple multivariate regression models based on extant great apes and humans to predict the maxillary landmarks from mandibular shape: one regression model pooling all extant species, as well as separate regression models for the extant species. We used principal component analysis to reduce the dimensions of the predictor variables; the regressions were computed in the subspace of the first seven principal components, which together explain more than 95% of the total sample variation. We used multiple reconstructions of the OH 7 maxillary dental arcade to assess the reconstruction uncertainty: one occlusal prediction and five statistical predictions (extant species pooled, *H. sapiens*, *P. troglodytes*, *G. gorilla*, and *Pongo* sp., respectively) for both mandibular reconstructions of OH 7. Our analyses therefore use 11 estimates of the OH 7 maxilla.

We assessed the reliability of our statistical approach by computing a maxillary prediction for every extant mandible on the basis of a cross-validated multiple multivariate regression model (pooling all extant species). A comparison of the actual maxillae to the predicted shapes (Extended Data Fig. 9) shows that the shape of the maxillary arcade can be predicted with high accuracy from the mandibular landmarks. When we applied the extant regression models to the two reconstructions of the OH 7 mandible the predicted maxillae look very similar to one another and

to the anatomical prediction dependent on crown occlusion (Extended Data Fig. 8m). These predicted maxillary shapes differ mostly in the size of the anterior dentition, reflecting the differences among the reference species. The overall arcade shapes of all 11 predictions, however, are almost identical.

**Comparisons within and between groups.** In order to provide a framework for interpreting the shape differences between fossil specimens we computed Procrustes distances between all possible individual pairs within extant species as a net dissimilarity measure for quantifying the large-scale shape differences. The pairwise Procrustes distances between early *Homo* fossil specimens are plotted in the context of frequency distributions of pairwise Procrustes distances among specimens intraspecifically and interspecifically (Fig. 2b, c, e). The 5% and 95% boundaries of the intraspecific distributions are plotted as vertical lines in the respective group colour.

In Fig. 2b, e and Extended Data Figs 4 and 5 fossils are not assigned group membership a priori. On the basis of these plots it is possible to assess the likelihood that the shape difference between two fossils can be found between any two humans, chimpanzees, orang-utans, or gorillas, and how it compares to the interspecific differences between any two representatives of these extant taxa. Pairwise comparisons of maxillary shape differences include the three predictions of the OH 7 maxilla (Fig. 2e) and, given separately, all five predictions based on individual hominid taxa (Extended Data Fig. 4f). These analyses do not make any assumptions whether a particular fossil is 'typical' for its species or an outlier. They are powerful in demonstrating major species differences, but similarity in arcade shape does not imply conspecificity unless other diagnostic morphology is consistent with the results.

In Fig. 2c we compared the frequency distributions of pairwise Procrustes distances within extant hominid mandibles to within-group distances for early *Homo* samples pooling different combinations of specimens attributed to *H. habilis* (OH 7, OH 13, KNM-ER 1802), *H. erectus* (Dmanisi specimens D2600, D2735, D211) and *H. rudolfensis* (KNM-ER 1482, KNM-ER 60000). For fossils the Procrustes distances between each pair of specimens are given, as well as smooth kernel histograms. For comparison we also simulated a mixed species sample by pooling *Pan troglodytes* and *Gorilla gorilla*; this illustrates the wide within-group distribution of a large mixed-species sample. As a yardstick for assessing the shape variation in fossil groupings we plotted the upper limit of the *G. gorilla* distribution as a dotted black line. Pooling different combinations of specimens attributed to *H. habilis*, *H. erectus* and *H. rudolfensis* yields within-group shape distances that far exceed those found in gorillas, the most variable extant apes.

We stress that our conclusions rest on the Procrustes distance within groups (that is, species). Here variation due to size allometry and neutral evolutionary divergence between populations is expected to be more important than variation due to adaptive divergence between populations (specimens belonging to the same biological species share the same functional adaptation).

**Size and allometry.** To assess the static allometric effects of jaw size on the shape of the dental arcade, we computed principal component (PC) analyses for both maxillary and mandibular dental arcades in Procrustes form space (Extended Data Fig. 7), and multivariate regressions of upper and lower jaw shape on the respective natural logarithms of centroid size within extant species. The statistical significance of the regression was tested using a permutation test based on the explained variance. In particular, we wanted to explore whether within extant species large mandibles are associated with a narrow dental arcade shape and more parallel post-canine tooth rows than in small mandibles (OH 7 and KNM-ER 1802 have large mandibles). In the Procrustes form space plots (Extended Data Fig. 7a–d) large jaws have low PC scores, and small jaws have high PC scores. As expected, the highly sexually dimorphic gorillas and orang-utans are more variable along PC 1 in Procrustes form space. For maxillary dental arcade shape allometry explains 4% of the total sample variation in *H. sapiens*, 9% in *P. troglodytes*, 18% in *G. gorilla* and 25% in *Pongo* sp. (all  $P < 0.001$ ). For mandibular dental arcade shape allometry accounts for 2% of the total sample variation in *H. sapiens*, 5% in *P. troglodytes*, 15% in *G. gorilla* and 21% in *Pongo* sp. (all  $P < 0.001$ ). In all species, these allometric effects are driven by the size of the canine (Extended Data Fig. 7e–l). These species differences in the fractions of variance explained by static allometry reflect the amount of sexual dimorphism. As expected, this percentage is smallest in humans, and largest in gorillas and orang-utans. Importantly, however, the static allometric effects of jaw size on arcade shape are negligible in all extant species.

**Occlusal prediction of the OH 7 maxillary dental arcade.** The maxillary dentition of KNM-ER 1590 was chosen as the best match in both size and morphology for the mandibular dentition of OH 7. The total mesiodistal crown length of the left C to M<sup>2</sup> is 612 mm in KNM-ER 1590 (ref. 34) and 592 mm in OH 7 (ref. 1). Silicone moulds were taken of the original teeth of KNM-ER 1590 (left I<sup>1</sup>, right and left C, P<sup>3</sup>, P<sup>4</sup>, M<sup>1</sup>, left M<sup>2</sup>), and cast in dental stone by one of us (MCD). A micro-CT based surface model of the left M<sup>2</sup> was mirror-imaged to obtain the right M<sup>2</sup>, and duplicate M<sup>2</sup>'s were used as surrogate M<sup>3</sup>'s. The right I<sup>1</sup> was adapted and modelled in wax from the preserved left I<sup>1</sup>, and I<sup>2</sup>'s were modelled, in proportion and size, on those

of OH 16 and KNM-WT 15000 to match the I<sup>1</sup>'s of KNM-ER 1590. The reconstruction of the OH 7 mandible was stereolithographically printed at 103% to obtain a good size match with the KNM-ER 1590 teeth.

A cast of the OH 7 mandibular dental arcade was mounted in an adjustable dental articulator (*Hanau*). The maxillary dentition was positioned one by one in edge-to-edge (anterior teeth) or centric occlusion (posterior teeth) using the vertical incisal pin to define the midline. Master casts were made of the completed maxillary dental arcade, first in epoxy-resin and then in dental stone. The latter was micro-CT scanned, and a surface model was reduced to 97% to obtain the correct size for the OH 7 mandible (Extended Data Fig. 6c).

**Reconstruction of the OH 7 parietals.** On the basis of the CT data a currently misaligned anterior fragment on the right parietal was restored to the published configuration<sup>1</sup> (Extended Data Fig. 10). Subsequently, we aligned the mirror-imaged right parietal fragment to the larger left side using the following criteria: (a) superimposition of left and mirror-imaged right asterion and mastoid angle; (b) alignment of the temporal lines on the left and mirror-imaged right parietal fragments; and (c) formation of a continuous sagittal suture. We mirror-imaged the thereby reconstructed left side to the right and aligned both sides. Vault curvature along the sagittal suture and remnants of the right parietal along the suture constrain this alignment and thereby the biparietal width of the resulting reconstruction (Extended Data Fig. 10c). For a second reconstruction (Extended Data Fig. 10d) we realigned the individual pieces that make up the left and right parietal sides. Cracks between the pieces were thereby diminished and the endocranial surfaces of the left and the mirror-imaged right parts could be better aligned, mostly because of the resulting changes in coronal curvature. Compared with the first reconstruction this version is narrower anteriorly and slightly broader posteriorly. Both reconstructions seem valid when different natural anatomical asymmetries are assumed. It has been suggested that the right parietal part, which preserves the occipital angle, could in fact be a left parietal of a second individual, preserving the frontal angle<sup>12</sup>. However, this suggestion is incompatible with the presence of a temporal line that turns inferiorly just anterior to the lambdoid suture (Fig. 3a). Measurements of the parietal reconstructions are given in Supplementary Note 5.

**Estimation of the ECV of OH 7.** To predict the ECV of OH 7 we quantified parietal size and shape of the two anatomical reconstructions as well as a comparative sample of extant hominids, and used regression-based and thin-plate-spline (TPS) geometric reconstruction methods.

**Quantification & sample.** On the basis of a published endocranial landmark set<sup>35</sup>, we defined 68 3D (semi-)landmarks located on the parietal endocranial surface of OH 7 (Extended Data Fig. 10e). The same subset was retrieved from a sample of 257 extant hominids (84 *H. sapiens*<sup>35</sup>, 55 *P. troglodytes*<sup>36</sup>, 54 *G. gorilla*<sup>37</sup> and 64 *Pongo* sp.<sup>37</sup>). Among these are 124 juveniles with at least M1 fully erupted to bracket the late juvenile age of OH 7. To validate our approach, we used several fossils with known ECVs (*Australopithecus africanus*: Sts 5, Sts 60, Sts 71, StW 505, MLD 37/38; *Homo habilis*: KNM-ER 1813; *Homo erectus*: KNM-ER 3733, KNM-ER 3883, KNM-WT 15000, OH 9). To gain point-to-point correspondence, semi-landmarks were allowed to slide to the landmark configuration on OH 7 (ref. 38). Subsequently we transformed the resulting coordinates into Procrustes shape variables<sup>39,40</sup> and computed Procrustes form variables that capture both shape and size information<sup>41</sup>.

**Regression model.** On the basis of the extant sample, we established a linear regression model (adjusted  $R^2 = 0.9908$ ) to estimate ECV from parietal endocranial form variables. The predicted ECV for the extant hominids is highly correlated to the actual ECV without a taxon-dependent bias towards over- or underestimation (Extended Data Fig. 10f). This also applies to the fossil specimens that were not part of the sample to establish the regression model.

**TPS reconstructions.** Assuming that each individual of the extant sample had only the parietal area preserved as in OH 7, we predicted the shape of its complete endocast based on TPS warping of all other individuals, and measured the ECV of the resulting 256 reconstructions for each individual. The predicted ECV (the mean of multiple estimates) is highly correlated to the actual ECV (Extended Data Fig. 10g). While there is less discrepancy of predicted versus actual ECV for humans as compared to the regression-based estimation method, the ECV of some species, especially gorillas, is consistently underestimated.

**ECV estimates of OH 7.** For both anatomical reconstructions of OH 7, we predicted the ECV based on the regression model and the multiple endocast reconstructions generated by TPS-warping. Given that only the parietals are preserved, the ECV estimates inevitably have high uncertainty, reported here as 95% single-prediction bands (regression) and the range of multiple estimates<sup>42</sup> (TPS reconstructions). For the first anatomical reconstruction, the regression-based and TPS-reconstruction-based estimates are 790 ml (678–921 ml) and 771 ml (663–907 ml), respectively, and for the second anatomical reconstruction the estimates are 729 ml (630–844 ml) and 824 ml (710–967 ml), respectively. We consider brain growth completed in individuals with the second molar and canine in occlusion<sup>43,44</sup>, and do not make corrections to obtain an adult value (contrary to ref. 1). We consider these values more

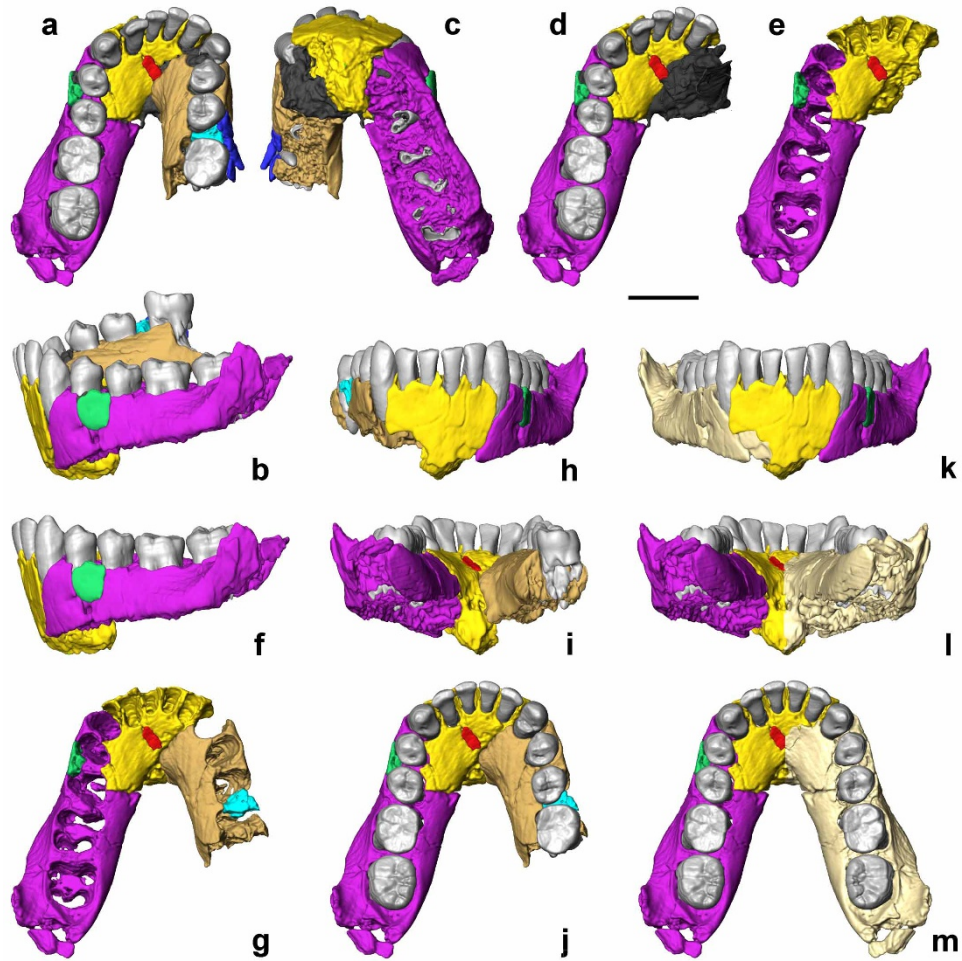


reliable than previous ones<sup>1,14–20</sup>: the (semi-)landmark-based quantification of parietal form is more accurate than the individual chords, arcs or volumes used previously; all data were taken from digital copies of the original specimens (avoiding problems of shrinkage or distortion of casts); the comparative sample is large and taxonomically diverse; particularly the regression-based method is not taxon-dependent; and methods were validated for fossil hominins with known ECVs.

**ECV comparison of OH 7, OH 13 & KNM-ER 1813.** *Sample.* *Homo sapiens* 1509 (refs 35, 45–47, Lewis J. E. & Meyer M., personal communication, 2014; worldwide populations). *Pan troglodytes* 184 (refs 48–50, McCarthy R., personal communication, 2005). *Gorilla gorilla* 101 (ref. 48, new data, McCarthy R., personal communication, 2005). *Pongo pygmaeus* 111 (refs 37, 48). *Pongo abelli* 34 (refs 37, 48). The human brain-weight data from ref. 47 were converted to millilitres, by correcting for the density of fresh brain tissue ( $1.036 \text{ g ml}^{-1}$  following ref. 48).

*Pairwise comparisons within groups.* In light of the large ECV differences between OH 7 (796 ml; 684–927 ml) and the potentially conspecific specimen KNM-ER 1813 (509 ml, ref. 19) we tested whether such ECV differences could be sampled from recent *H. sapiens*, *P. troglodytes*, *P. pygmaeus*, *P. abelli* and *G. gorilla*. We compared ECVs of all possible pairs of individuals within extant groups, and divided the smaller by the larger value; the corresponding frequency distributions and their 5% boundaries are shown in Fig. 3c. This figure also compares OH 7 and OH 13 (650 ml, ref. 20), as well as OH 13 and KNM-ER 1813.

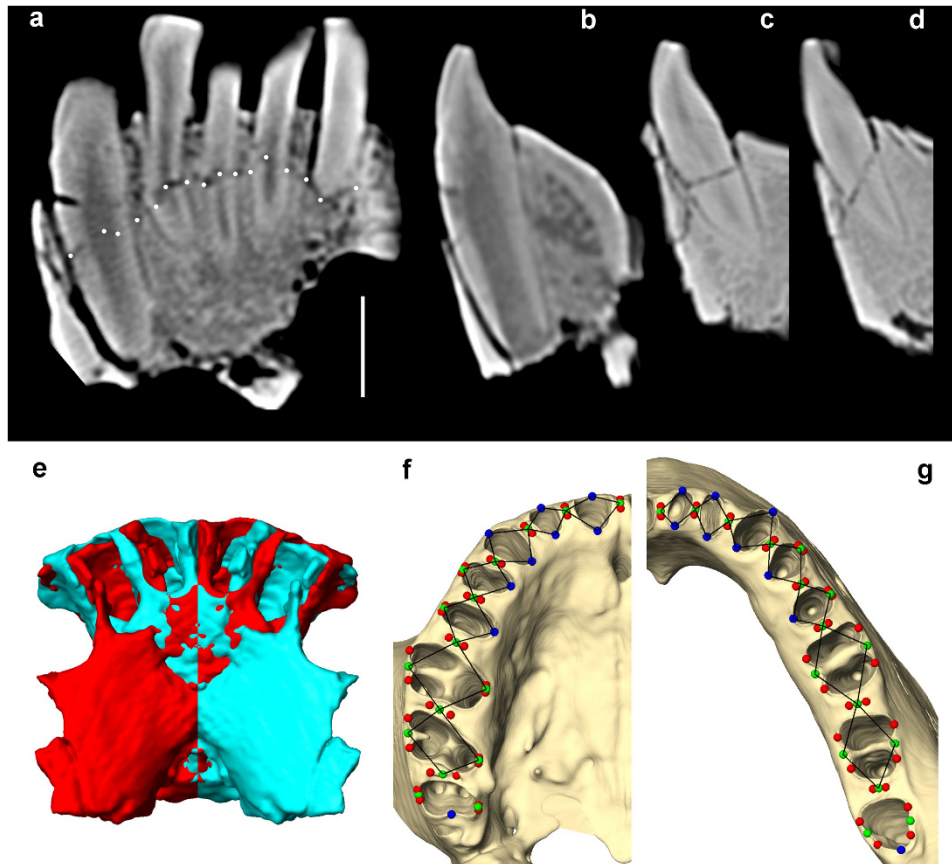
29. Clarke, R. J. A *Homo habilis* maxilla and other newly-discovered hominid fossils from Olduvai Gorge, Tanzania. *J. Hum. Evol.* (2012).
30. Gunz, P., Mitteroecker, P., Neubauer, S., Weber, G. W. & Bookstein, F. L. Principles for the virtual reconstruction of hominin crania. *J. Hum. Evol.* **57**, 48–62 (2009).
31. Kimbel, W. H. & Rak, Y. The cranial base of *Australopithecus afarensis*: new insights from the female skull. *Phil. Trans. R. Soc. B* **365**, 3365–3376 (2010).
32. Mardia, K. V., Bookstein, F. L. & Moreton, I. J. Statistical assessment of bilateral symmetry of shapes. *Biometrika* **87**, 285–300 (2000).
33. Rohlf, F. J. & Slice, D. Extensions of the Procrustes method for the optimal superimposition of landmarks. *Syst. Zool.* **39**, 40–59 (1990).
34. Wood, B. A. *Koobi Fora Research Project, vol. 4. Hominid Cranial Remains.* (Clarendon Press, 1991).
35. Neubauer, S., Gunz, P. & Hublin, J. J. The pattern of endocranial ontogenetic shape changes in humans. *J. Anat.* **215**, 240–255 (2009).
36. Neubauer, S., Gunz, P. & Hublin, J. J. Endocranial shape changes during growth in chimpanzees and humans: a morphometric analysis of unique and shared aspects. *J. Hum. Evol.* **59**, 555–566 (2010).
37. Scott, N., Neubauer, S., Hublin, S. & Gunz, P. A shared pattern of postnatal endocranial development in extant hominoids. *Evol. Biol.* **41**, 572–594 (2014).
38. Gunz, P., Mitteroecker, P. & Bookstein, F. L. in *Modern Morphometrics in Physical Anthropology* (ed. Slice, D. E.) 73–98 (Kluwer Academic/Plenum Publishers, 2005).
39. Gower, J. C. Generalized Procrustes analysis. *Pyschometrika* **40**, 33–51 (1975).
40. Rohlf, F. J. & Slice, D. Extensions of the Procrustes method for the optimal superimposition of landmarks. *Syst. Zool.* **39**, 40–59 (1990).
41. Mitteroecker, P., Gunz, P., Bernhard, M., Schaefer, K. & Bookstein, F. L. Comparison of cranial ontogenetic trajectories among great apes and humans. *J. Hum. Evol.* **46**, 679–697 (2004).
42. Neubauer, S., Gunz, P., Weber, G. W. & Hublin, J. J. Endocranial volume of *Australopithecus africanus*: new CT-based estimates and the effects of missing data and small sample size. *J. Hum. Evol.* **62**, 498–510 (2012).
43. Leigh, S. R. Brain growth, life history, and cognition in primate and human evolution. *Am. J. Primatol.* **62**, 139–164 (2004).
44. Leigh, S. R. Brain size growth and life history in human evolution. *Evol. Biol.* **39**, 587–599 (2012).
45. Lewis, J. E. *et al.* The mismeasure of science: Stephen Jay Gould versus Samuel George Morton on skulls and bias. *PLoS Biol.* **9**, e1001071 (2011).
46. Brown, P. Australian & Asian Palaeoanthropology; Research resources. <http://www.peterbrown-palaeoanthropology.net> (2014).
47. Marchand, F. *Über das Hirngewicht des Menschen.* (Teubner, Leipzig, 1902).
48. Isler, K. *et al.* Endocranial volumes of primate species: scaling analyses using a comprehensive and reliable data set. *J. Hum. Evol.* **55**, 967–978 (2008).
49. Zuckerman, S. Age-changes in the chimpanzee, with special reference to growth of brain, eruption of teeth, and estimation of age; with a note on the Taung ape. *Proc. Zool. Soc. Lond.* **1**, 1–42 (1928).
50. Neubauer, S., Gunz, P., Schwarz, U., Hublin, J.-J. & Boesch, C. Brief communication: endocranial volumes in an ontogenetic sample of chimpanzees from the Tai Forest National Park, Ivory Coast. *Am. J. Phys. Anthropol.* **147**, 319–325 (2012).
51. van der Merwe, N. J., Masao, F. T. & Bamford, M. K. Isotopic evidence for contrasting diets of early hominins *Homo habilis* and *Australopithecus boisei* of Tanzania. *S. Afr. J. Sci.* **104**, 153–155 (2008).



**Extended Data Figure 1 | Reconstruction of the OH 7 mandible.** **a–e**, As preserved in occlusal view (**a**), left lateral view (**b**), inferior view (**c**), without the right corpus, showing the matrix fill (**d**), without the right corpus, matrix and dentition (**e**). **f**, Reconstruction in left lateral view without the right corpus. **g**, Occlusal view of corpus only. **h–j**, Full reconstruction in anterior view (**h**),

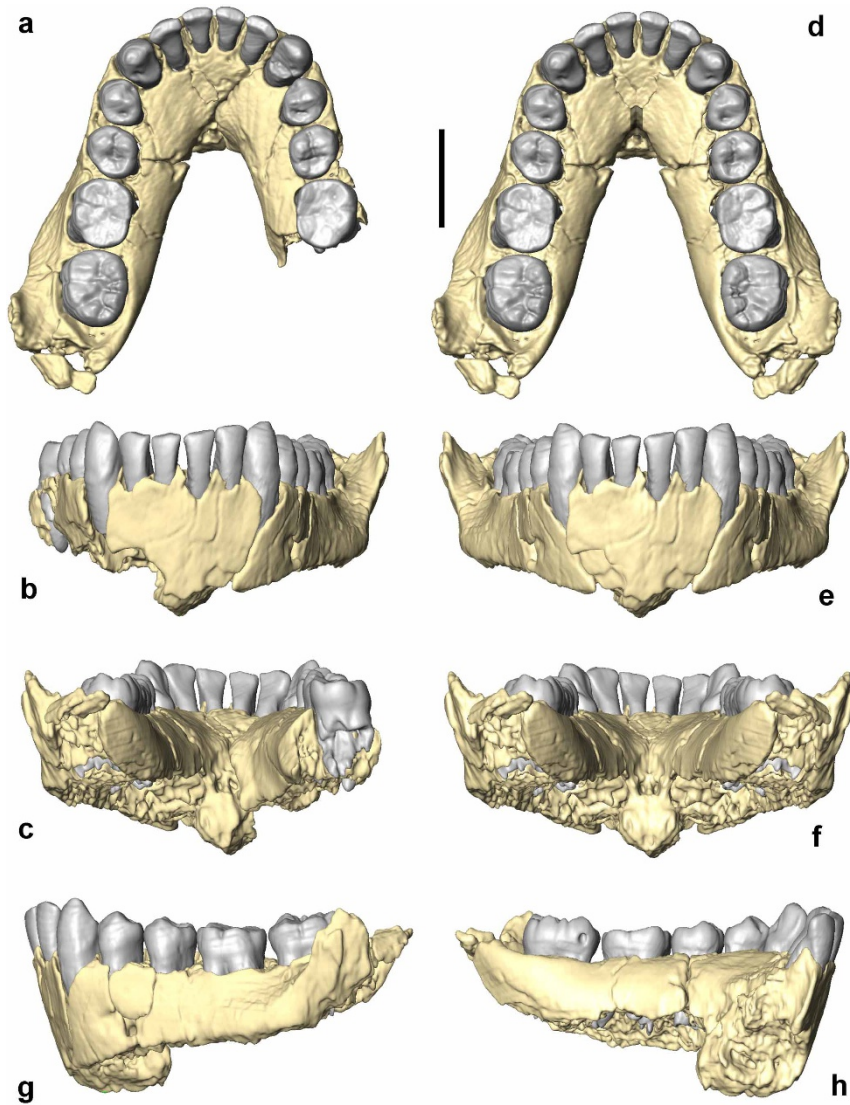
posterior view (**i**) and occlusal view (**j**). **k–m**, Reconstruction using the mirror-imaged left corpus in anterior view (**k**), posterior view (**l**) and occlusal view (**m**). Parts are colour-coded as described in the Supplementary Methods. Scale bar is 2 cm.





**Extended Data Figure 2 | The OH 7 anterior corpus and landmarks of the dental arcade.** **a**, Coronal CT section of the anterior corpus showing, from left to right, the roots of the left C to the right I<sub>2</sub>, as well as the course of the irregular transverse fracture marked by white dots. **b–d**, Labiolingual CT sections through the left C (**b**), I<sub>2</sub> (**c**) and I<sub>1</sub> (**d**). All three show the fracture, and **b** shows the open C root and closed apical alveolar wall. **e**, Anterior corpus as preserved (red) compared with a copy mirror-imaged across the midsagittal plane used for the reconstruction (cyan). The canine alveoli and the anterior

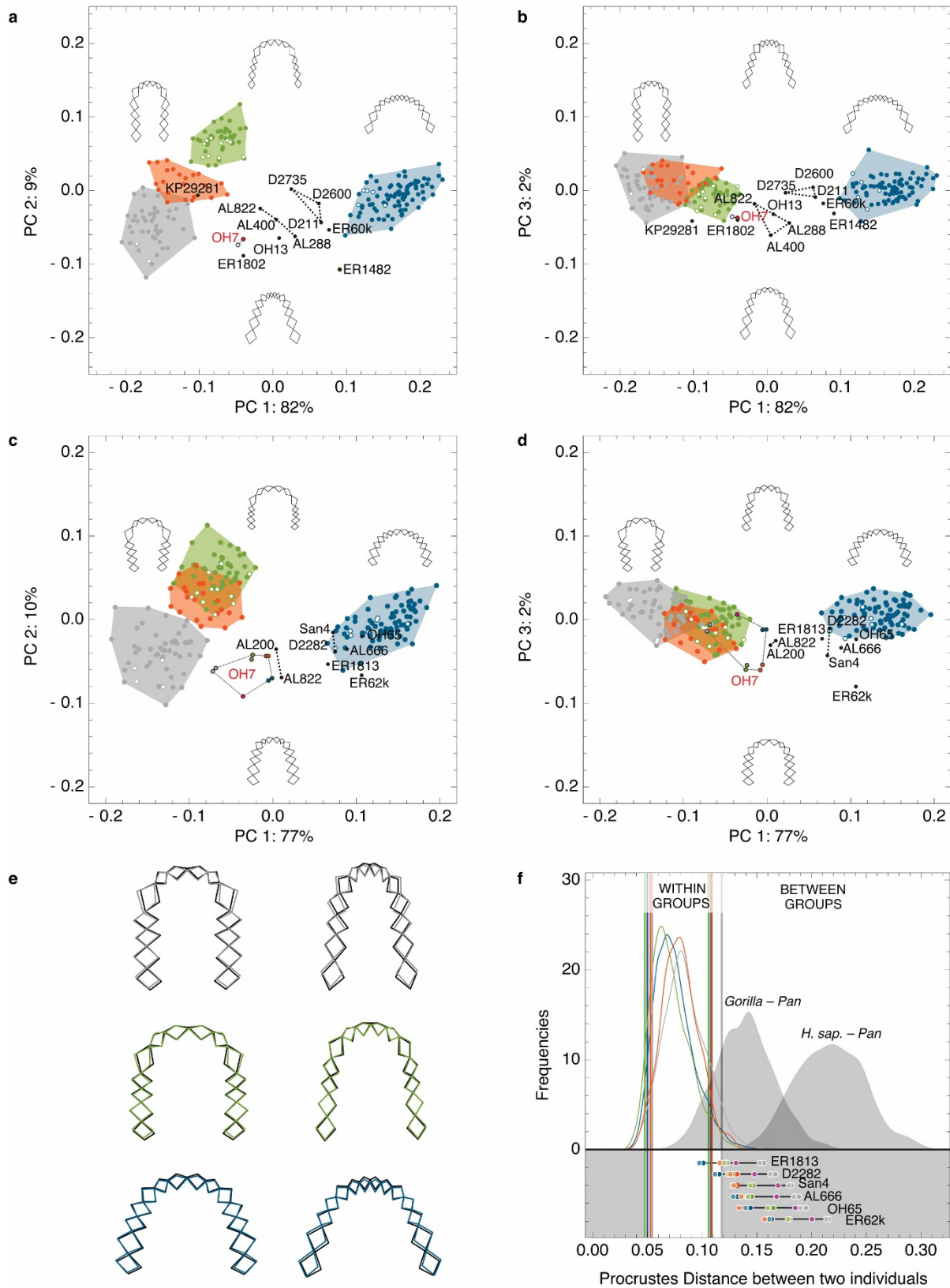
symphyseal surface of both sides match well, indicating a lack of overall plastic deformation. The plastically deformed interalveolar septa of the incisors reflect the dislocation of these teeth. Scale bar for **a–e** is 1 cm. **f, g**, Right maxilla (**f**) and mandible (**g**) of a modern human, showing the landmark positions. Full data sets include both sides of the arcade. Blue and red landmarks were taken from the specimens. The green landmarks were obtained by averaging pairs of red ones, and these were analysed with the blue ones to represent the arcade from left to right M2 (wireframe).



**Extended Data Figure 3 | The reconstructed OH 7 mandible.**

**a–c**, Reconstruction using the right corpus in occlusal (**a**), anterior (**b**) and posterior (**c**) view. **d–f**, Reconstruction on the basis of mirror-imaged left corpus in occlusal (**d**), anterior (**e**) and posterior (**f**) view. **g, h**, Reconstruction

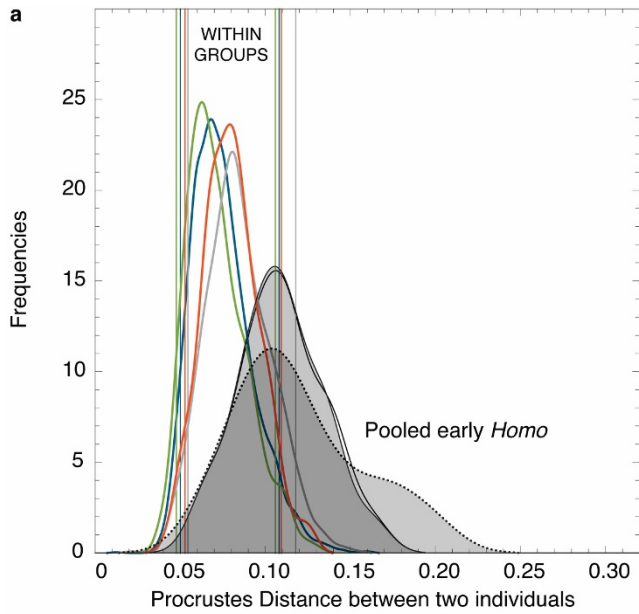
without right corpus in left lateral view (**g**) and left medial view (**h**). The hole visible on the lingual crown face of the left  $M_2$  was made to sample tooth enamel for isotope studies<sup>51</sup>. Scale bar is 2 cm.



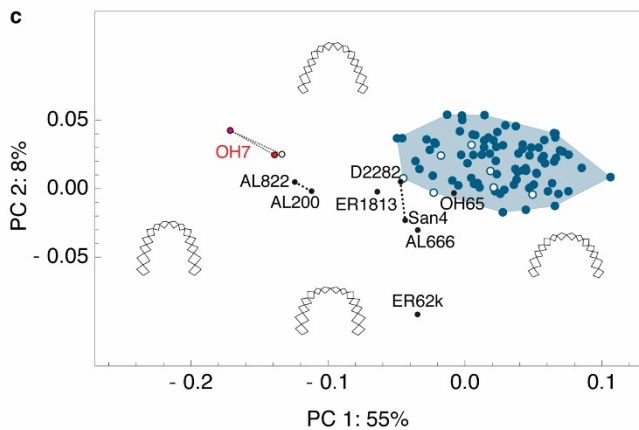
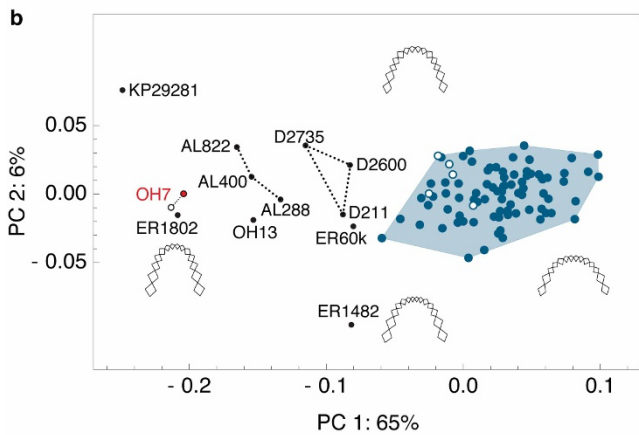
**Extended Data Figure 4 | Shape analysis of mandibular and maxillary dental arcades.** Group colour codes as in Fig. 2. **a–d**, Principal component analysis showing plots of mandibular dental arcade (**a**, PC 1 and PC 2; **b**, PC 1 and PC 3), and maxillary dental arcade (**c**, PC 1 and PC 2; **d**, PC 1 and PC 3). The convex hulls of the extant samples are given, with late juveniles shown as open circles. Wireframes show the shape changes associated with the respective PC axes three standard deviations away from the mean. **e**, Superimposed mean shapes of late juveniles (black) and adults (group

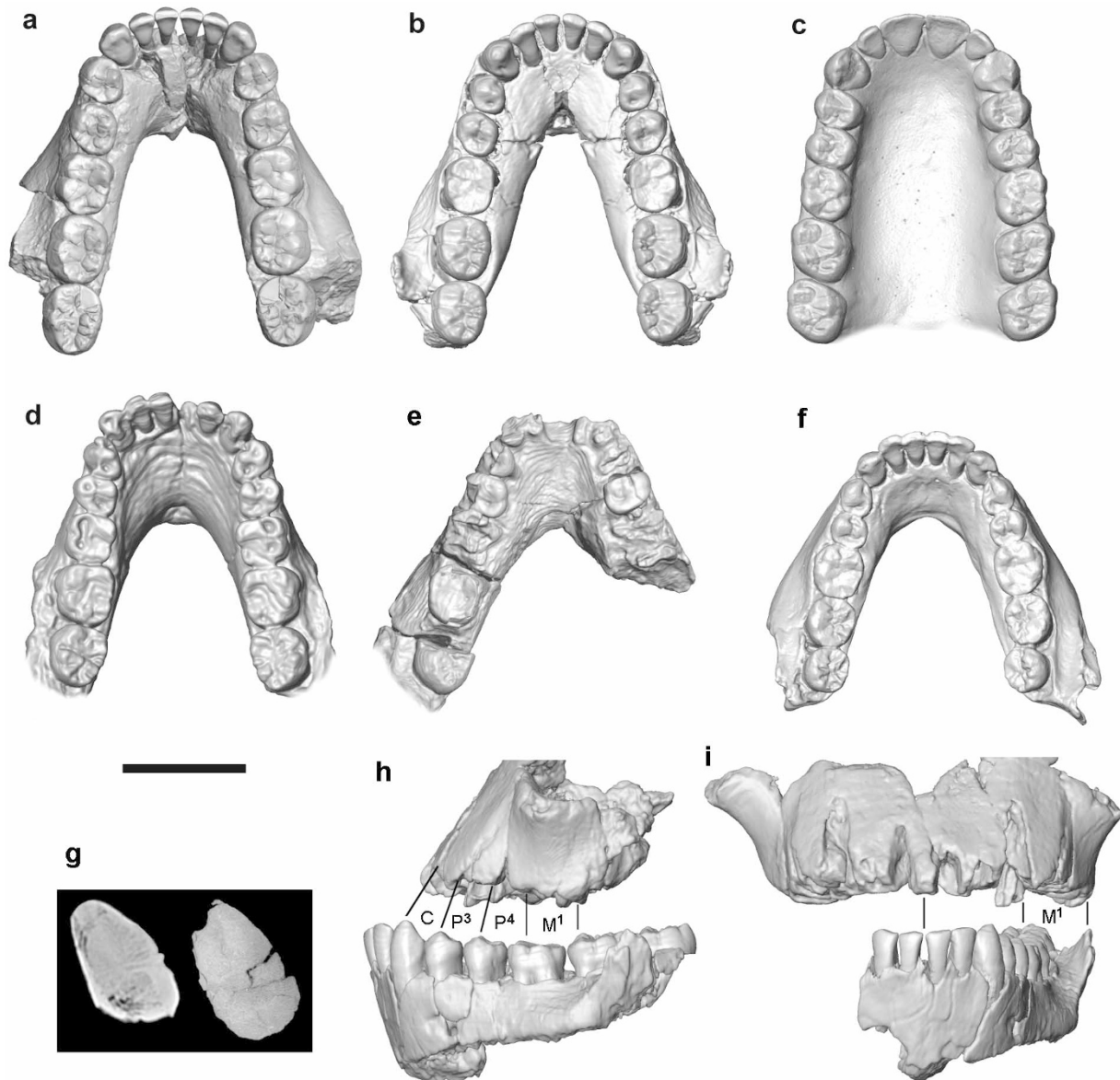
colour); maxillary (left) and mandibular (right) dental arcade of *Gorilla gorilla*, *Pan troglodytes* and *Homo sapiens*. **f**, Pairwise Procrustes distances between the nine different maxillary reconstructions of OH 7 and other early *Homo* maxillae: eight statistical predictions are plotted in the colour of the reference species, one occlusal prediction (purple). Frequency plots of the Procrustes distances between all possible individual pairs within (group colour) and between groups (grey); lines represent the 5% limits and 95% limits of these distributions, respectively.





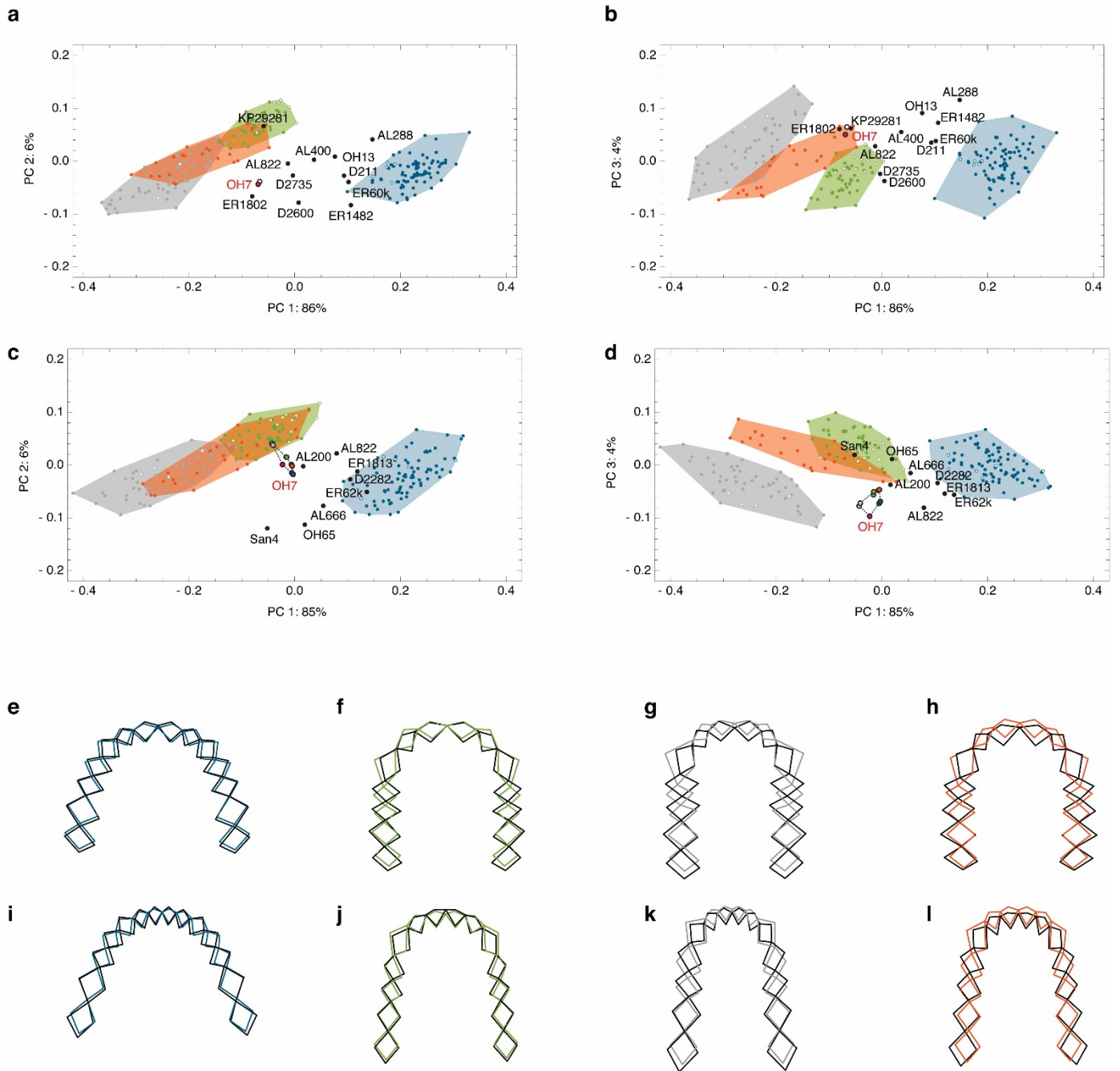
**Extended Data Figure 5 | Shape analysis of mandibular and maxillary dental arcades.** **a**, Frequency plot of the maxillary shape differences between all pairs within extant groups (colours as in Fig. 2) and within the pooled sample of early *Homo* fossils (black solid lines using statistical predictions of the OH 7 maxilla, dotted line using the occlusal prediction). **b–c**, Principal component analyses showing plots of the mandibular (**b**) and maxillary (**c**) dental arcades. Recent *Homo sapiens* are plotted in blue; late juveniles are shown as open circles. Wireframes show the shape changes associated with the respective principal component axes three standard deviations away from the mean. The red and open circles represent the two alternative mandibular reconstructions of OH 7 (**b**), and the respective statistical predictions of the maxillary dental arcade based on occlusion is plotted in purple (**c**).





**Extended Data Figure 6 | Comparisons of OH 7 mandible.** a–f, Occlusal view of KNM-ER 1802 (a), OH 7 (b), OH 7 maxillary dental arcade (occlusal prediction) (c), A.L 400-1 (d), KNM-ER 1482 (e) and D211 (f). g, Midsagittal CT sections of the symphyses of OH 7 (left) and KNM-ER 1802 (right) showing similar ovoid cross-sectional shapes. h, Left lateral view of KNM-ER 1470 and OH 7, aligning the reliably identifiable M1 crown position with the

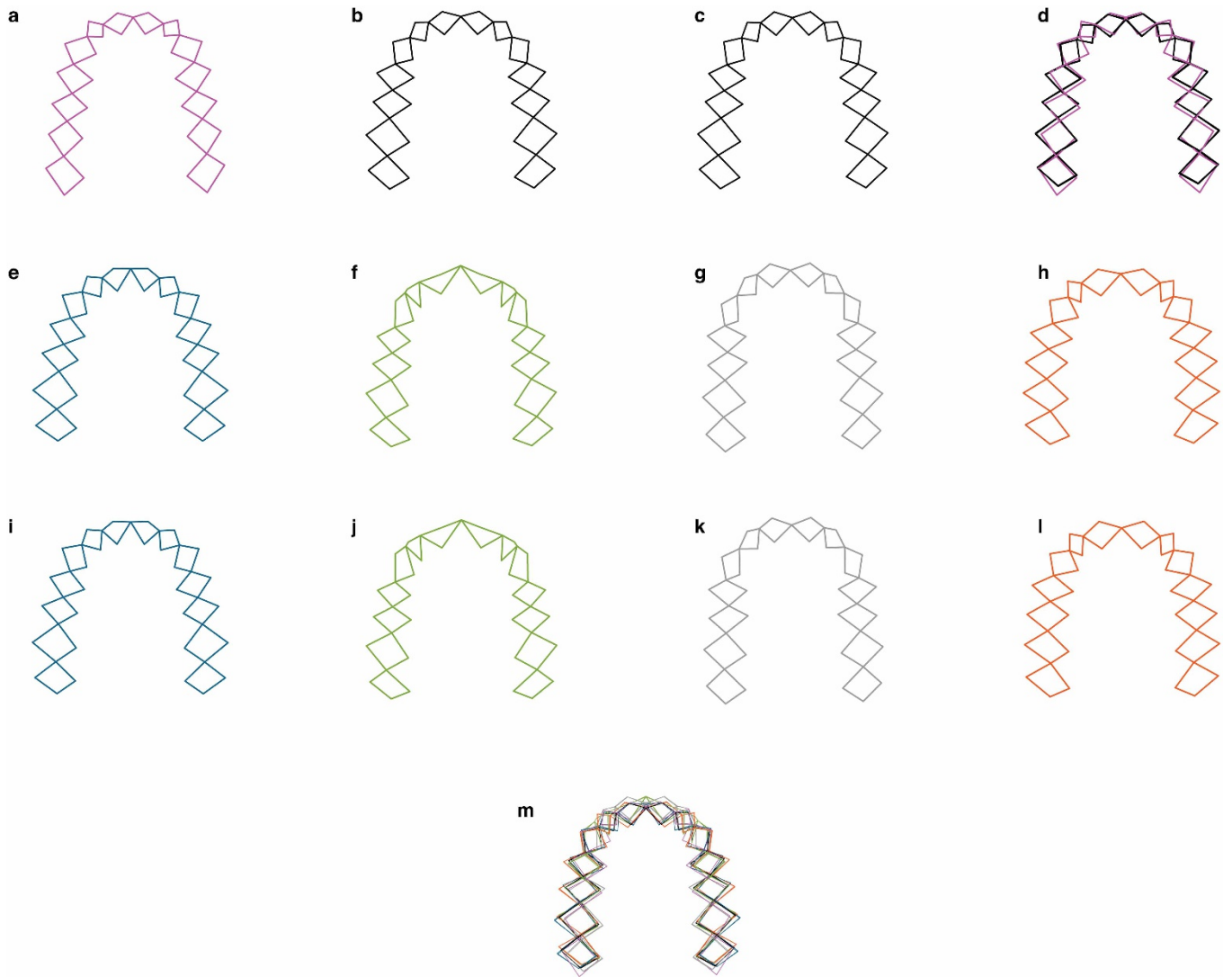
corresponding part of the OH 7 row. For C to P4 lines link alveolar margins and corresponding crown position along the OH 7 row. i, Anterior view aligning KNM-ER 1470 and OH 7 by their midsagittal plane. KNM-ER 1470 is marked by a shorter C–M<sup>1</sup> row, and a non-projecting anterior row but a wider dental arcade, shown by the position of its left M<sup>1</sup> alveolus well lateral to the corresponding part of OH 7. Scale bar is 3 cm.



**Extended Data Figure 7 | Allometry and dental arcade shape.** a–d, Principal component analysis in Procrustes form space of mandibular dental arcade (a, PC 1 and PC 2; b, PC 1 and PC 3) and maxillary dental arcade (c, PC 1 and PC 2; d, PC 1 and PC 3). Colour codes as in Fig. 2. A multivariate regression model was used to assess the covariation of dental arcade shape with size

(log centroid size) within extant groups. e–l, Wireframes show shape predictions for smallest (black) and largest (group colour) centroid size for upper (e–h) and lower (i–l) jaw of *H. sapiens* (e, i), *P. troglodytes* (f, j), *G. gorilla* (g, k) and *Pongo* (h, l). The allometric effects of jaw size on arcade shape are negligible.

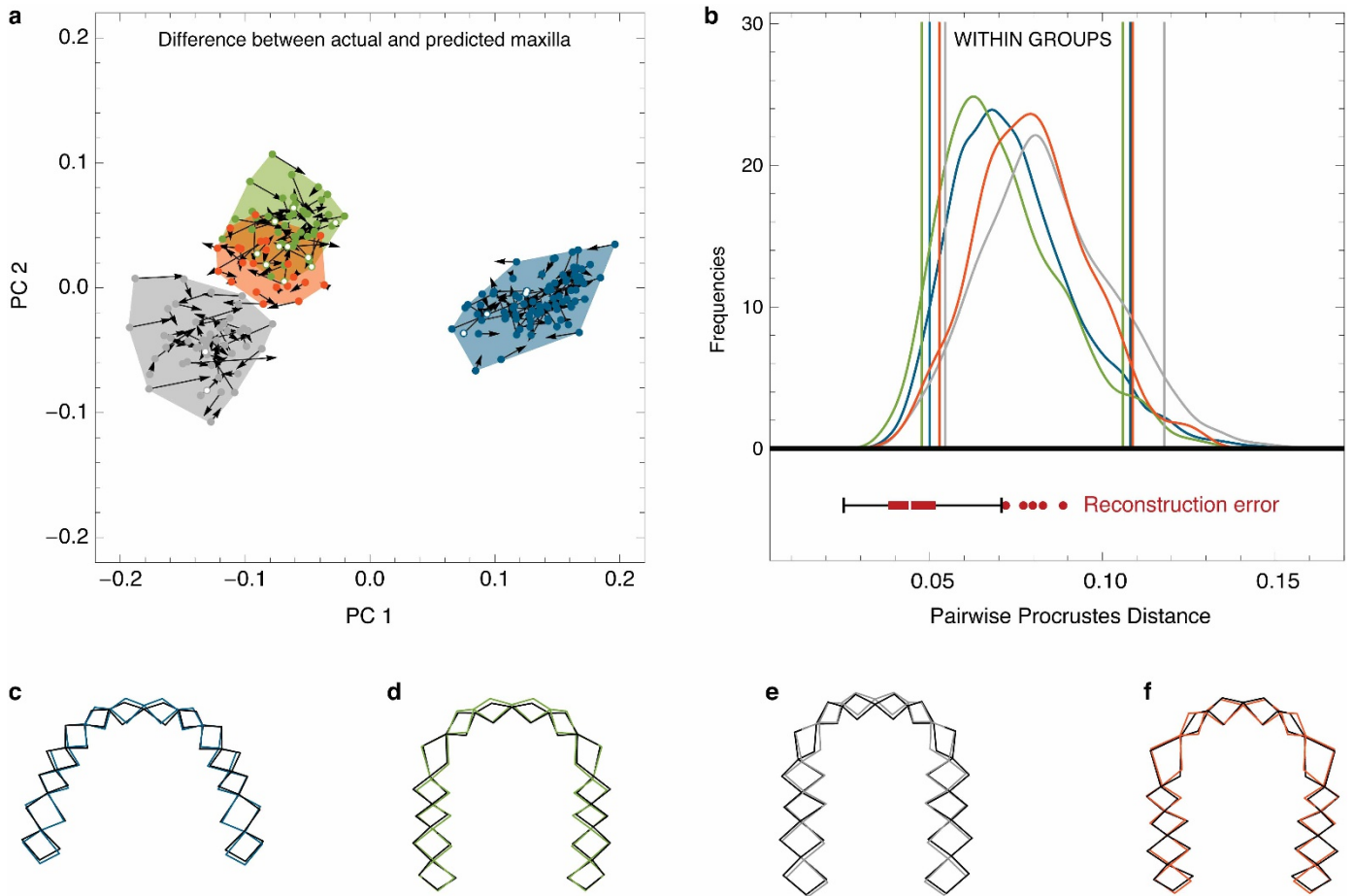




**Extended Data Figure 8 | Wireframes of maxillary dental arcades.**

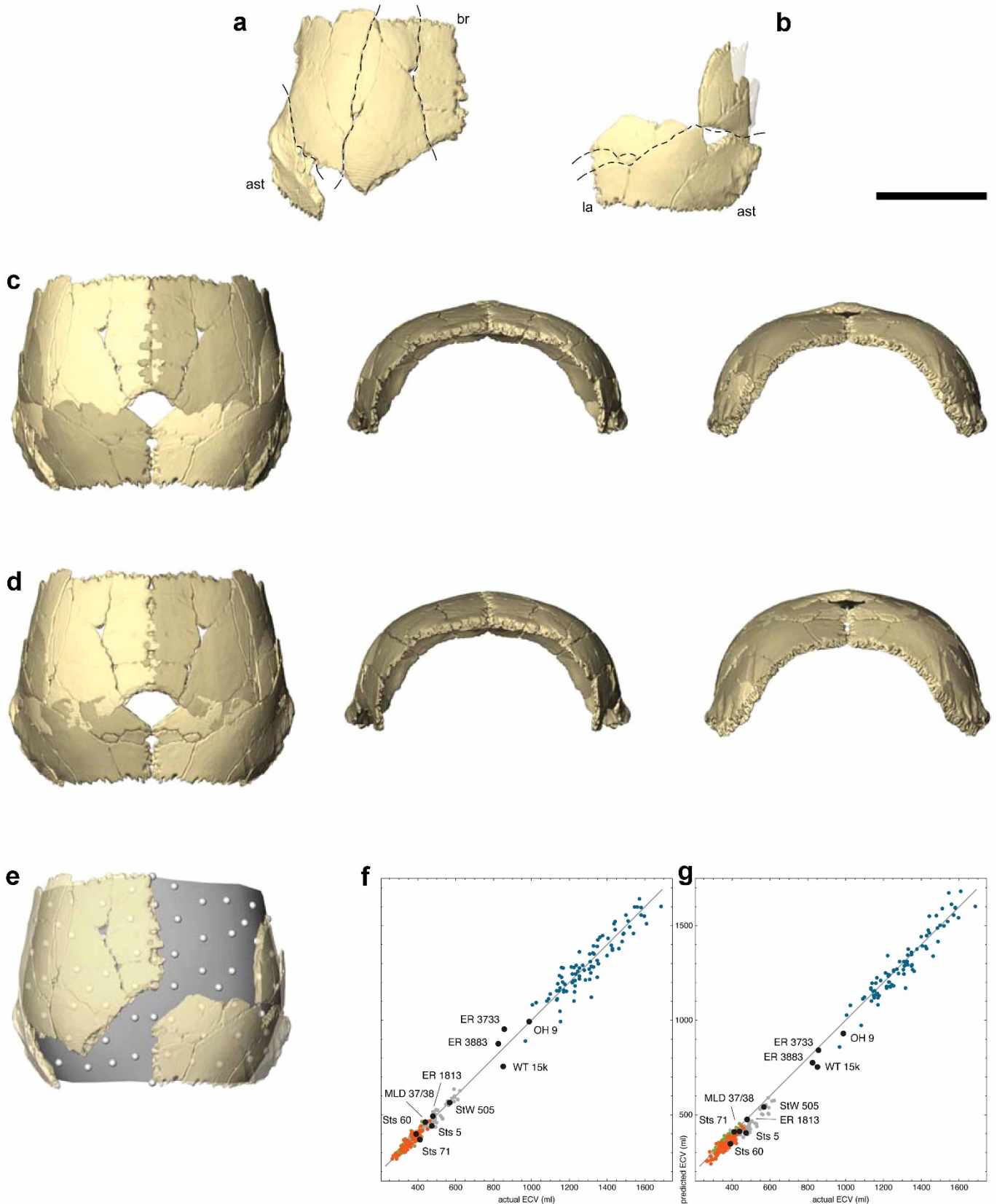
**a**, Predicted OH 7 maxillary arcade, based on dental occlusion. **b, c**, Statistical predictions for OH 7 maxilla based on two alternative mandibular reconstructions using a regression model based on all extant species. **d**, Three maxillary predictions of OH 7 (**a–c**) superimposed. **e–l**, Statistical predictions

of OH 7 maxillary dental arcade based on separate regression models for each extant species (applied to two alternative reconstructions of the OH 7 mandible). **e, i**, *H. sapiens*; **f, j**, *P. troglodytes*; **g, k**, *G. gorilla*; **h, l**, *Pongo* sp. **m**, All predictions of the OH 7 maxillary dental arcade superimposed.



**Extended Data Figure 9 | Reconstruction uncertainty of the maxillary dental arcade.** **a**, For every extant specimen we predicted the shape of the maxillary arcade from the mandibular landmarks using a multivariate regression model. Arrows show the difference between the actual and the predicted maxilla in the space of the first two principal components. Colour codes as in Fig. 2. **b**, Box and whisker chart of the Procrustes distances between original and predicted maxillae in the context of the pairwise Procrustes distances within extant groups. Shape differences between original and

prediction are usually much smaller than typical within-group shape differences. Even the five outliers with the largest 'reconstruction errors' fall well within the range of shape differences within groups. **c–f**, Representative examples of the actual (black) versus predicted (group colour) maxilla wireframes, given for one individual each of: **c**, *Homo sapiens*; **d**, *Pan troglodytes*; **e**, *Gorilla gorilla*; **f**, *Pongo* sp. These predictions use a regression model based on all extant species together.



**Extended Data Figure 10 | OH 7 parietal reconstructions and ECV estimation.** **a, b**, Left and right parietals, with bregma (br) and lambda (la) and asterion (ast) indicated. Dashed lines demarcate pieces that were realigned for the second reconstruction. The transparent part of right parietal represents the current, incorrect alignment, corrected for both reconstructions. **c**, First anatomical reconstruction in (left to right) superior, anterior and posterior view, combining the left and right side without realignment of smaller parts

(mirror-imaged pieces in darker shade). **d**, Second anatomical reconstruction in (left to right) superior, anterior and posterior view, based on additional realignment of smaller parts. **e**, Endocranial (semi-)landmarks quantifying parietal form. Scale bar, 5 cm. **f**, Regression-based ECV estimates plotted against actual values; grey line indicates perfect match between predicted and actual ECVs; group colours as in Fig. 3 and fossils in black. **g**, Predicted ECVs from TPS reconstructions plotted against actual values.